ISSN 2621-5683
ELIPSOIDA Vol 03 No 01, Juni 2020 (46-54)
@Departemen Teknik Geodesi UNDIP
ELIPSOIDA
Jurnal Geodesi dan Geomatika

OPAK FAULT DEFORMATION MONITORING USING SENTINEL-1 INSAR DATA FROM 2016-2019 IN YOGYAKARTA INDONESIA

Bondan Galih Dewanto*[1], Mohamad Bagas Setiawan [2], Gilang Cahya Nusantara[3]
*Email: bondan.galih.d@mail.ugm.ac.id
[1] Center for Disaster Studies, Universitas Gadjah Mada, Yogyakarta, Indonesia
[2] Department of Geodetic Engineering, Faculty of Engineering, Universitas Gadjah Mada, Indonesia
[3] Senior High School 2 Wonosari, Yogyakarta, Indonesia

(Diterima 5 Mei 2020, Disetujui 3 Juli 2020)

ABSTRACT

The 2006 Yogyakarta earthquake occurred at 05.55 West Indonesia Time, May 27, 2006 with a magnitude of M_w 5.9. The earthquake had a great trauma effect for the community because there were many fatalities, around 6,000 people died. Therefore, it is very important to perform a research conduct research to determine the deformation that is currently happening around the Opak Fault. In this research, during 2016-2019, we collected products for Sentinel-1 synthetic aperture radar interferometry (InSAR) to measure the current fault deformation. The InSAR data was processed using LiCSBAS, a time series analysis kit of open-source SAR interferometry (InSAR) that integrates with the automated Sentinel-1 InSAR processor (LiCSAR). In the processing scheme for LiCSBAS, interferograms with many unwrapping errors are automatically detected and removed via loop closure. Reliable time series and velocities are extracted using several noise indices with the help of masking. The location of the Opak Fault can be detected clearly in the result because the deformation pattern around the fault is contrary different. The west of Opak Fault shows an uplift movement, while the deformation occurred in the east area of the fault shows subsidence movement.

Keywords : Opak Fault, Crustal Deformation, Sentinel-1 InSAR Data, LiCSBAS

1. INTRODUCTION

Java Island is one of the archipelagic arc products of the above-mentioned convergent interactions that took place from the Cretaceous Period (100-65 million years) and is still valid until now. As researchers well know and show, plate tectonic activity in the form of convergent interactions between the Indian-Australian Ocean Plate slides down the Sunda Shelf, which is part of the plate forming an archipelago of the Eurasian continent (Hamilton, 1979).

Satellite observation is a crucial resource for Earth observation, enabling, in particular, the prevention of the effects of natural hazards. It provides several advantages over other monitoring techniques: data collection in inaccessible areas; comprehensive coverage allowing a complete study of global phenomena; and the availability of long-term historical data for wide areas, enabling the phenomena to be analyzed temporally. Additionally, it outperforms in situ data collection, which is typically more costly and sluggish.

Opak River is situated in Java Island's Bantul District Yogyakarta with a general pattern from Southwest to Northeast, where it occupies the Merapi sediment volcanic fluvium west of Gunungkidul, where this river's existing is assumed to reflect an error. Based on the basis of a catalog reported by the Center for Volcanology and Geological Disaster Reduction, the Yogyakarta Region and its surrounding areas experienced many earthquake events that damaged buildings and claimed injuries among them; (1) In 1840 an earthquake was recorded (2) An earthquake on 10 June 1867 claimed the lives of 5 people, at an intensity scale of approximately IX MMI with damage; (3) Respectively, on 23 July 1943 tectonic earthquakes occurred in Yogyakarta, Klaten and Surakarta with the same intensity scale of IX MMI damaged houses, swallowing 213 lives, and injuring 2096 people. (4) On 13 January 1981, tectonic earthquakes emerged again from subduction activity. The Ambarrukmo Hotel's base sustained a fracture as a consequence of this earthquake, and several buildings encountered wall cracks. The strength of the Earthquake was measured at MMI VI. (5) On 27 May 2006, the last earthquake occurred on land, resulting in significant damage to buildings in the Bantul, Prambanan, and Klaten regions, including Yogyakarta. More than 5,600 people exceeded the death toll. Earthquakes in 2010 (6) and 2015 (7) were also felt in Yogyakarta.

In the previous study, Tsuji *et al.* (2009) monitored the deformation around Opak Fault which is located in Opak River due to 2006 Yogyakarta earthquake. The results demonstrate that the surface deformation occurred ~10 km east

of the Opak River fault thought to be the source of the May 2006 event and that the probable causative fault delineated in this study is consistent with the aftershock epicenters determined by a temporary seismic network. The trace of the causative fault bends at its southern termination toward the Opak River fault as if it were a splay. Interferograms spanning the May 26 2006 Java earthquake suggest an area of about 7.5 km^2 of subsidence (~2 cm) and incoherence south of the city of Yogyakarta that correlates with significant damage to housing, high modeled peak ground accelerations, and poorly consolidated geologic deposits (Poland, 2010). The subsidence and incoherence is inferred to be a result of intense shaking and/or damage.

This paper explains surface deformation observed using InSAR analysis during the period 2016-2019. The output is the field of velocity and time series, due to data in the region around Opak Fault.

2. LITTERATURE REVIEW

2.1 Tectonic Background

Many of the world's major earthquakes have occurred in subduction zone settings, where significant events greater than M_w 8 have ruptured hundreds of kilometers from the main epicenter (Lay, 2015). There have been significant scientific efforts to clarify the climate in the context of plate tectonics about the frequency of these events. Geodetic studies have shown signatures of elastic strain energy accumulation on subduction megathrusts, in addition to the long-term rotation of tectonic plates, in which regions of strong coupling during interseismic cycles were used to expose stress buildup where seismic ruptures are likely to occur (Loveless and Meade, 2010). On the other hand, slipping at subduction zones can also be accommodated on creeping areas inside the seismogenic zone and/or transition zone below the top 40 km (Wallace and Beavan, 2010).

The Java subduction zone is one of the world's most tectonically active plate boundaries, stretching from the Sunda Strait to eastern Indonesia for around 1700 km. The lack of large megathrust earthquakes (M_w > 7.8) is a distinctive characteristic of this subduction. Historical records indicate that there have been few, if any, major earthquakes on the Java megathrust (Newcomb and McCann, 1987). Over the entire instrumental seismological era, the largest earthquakes reported offshore Java island were the 1994 Mw 7.8 and 2006 Mw 7.7 events which were identified as classical tsunami earthquakes by various studies (Abercrombie *et al*., 2001). This suggests that either the slip on the Java megathrust is dominantly aseismic and there is insufficient elastic strain accumulation to generate significant megathrust earthquakes, or that the earthquakes in this boundary have recurrence times beyond the span of the observational period. The lessons learned from the Sumatra 2004 and Tohoku 2011 earthquakes show that the lack of recognized large earthquakes in a subduction zone does not preclude the possibility of future large earthquakes.

The earthquake for the people of Indonesia is one of the frightening natural disasters because it can cause damage to land and buildings. The 2006 earthquake in the Special Region of Yogyakarta was a tectonic earthquake caused by an active fault (fault) in Opak River, Imogiri District, Bantul Regency. The existence of the Opak Fault has indeed been predicted by geologists and is contained in the Geology Map of Yogyakarta P3G Bandung output in 1977 and updated in 1995. However, this fault became more popular after the earthquake in Yogyakarta and Central Java on May 27, 2006, because some geologists thought the earthquake was caused by the activation of the Opak Fault. Abidin *et al*. (2009) analyzed the 2006 Yogya earthquake coseismic deformation in a horizontal and vertical motion of about 10-15 cm. Horizontal deformation after seismic ranges from 0.3-9.1 cm. They concluded the location of the fault causing the Yogyakarta earthquake was in the east of the Opak river about 5-10 Km. This fault has an upright dip of almost 90° with the direction of N48E as the strike, moving as a strike-slip fault.

2.2 Synthetic Aperture Radar Interferometry (InSAR)

Interferometric Synthetic Aperture Radar (InSAR) has been successfully applied to the field of ground deformation research in many countries, and has shown great capacity to track high-spatial and temporal resolution subsidence disasters in recent decades (Massonnet and Feigl, 1998). InSAR is a method that two radar scenes acquired at different times in the same region which may provide information about the radar process.

Nevertheless, spatial-temporal decorrelation and atmospheric delay usually affect the accuracy of the InSAR measurement (Atzori *et al.*, 2009). Then, Persistent Scatter Interferometry (PS-InSAR) and Small Baseline Subset InSAR (SBAS-InSAR) are proposed to increase accuracy (Trasatti *et al.*, 2008). The SBAS-InSAR system not only eliminates spatial and temporal decorrelation, but also phase unwrapping and errors in atmospheric delay. Therefore, it could have reliable features for a deformation time series (Lanari *et al*., 2007).

Manunta *et al.* (2008) used satellite radar data from the European Space Agency (ERS)-1/2 to detect large-scale deformation in Rome, Italy, and then demonstrated the ability of the SBAS method to obtain similar information from low-resolution InSAR data, which led to the identification of several sites affected by major displacements. Zhou *et al.* (2017) used 15 Sentinel-1A TOPS SAR images with the SBAS-InSAR technique to examine the wide area surface subsidence characteristics in Wuhan, China. The result showed that the time series of surface subsidence posed nonlinear subsidence with significant seasonal variations, which established the spatial-temporal characteristics of wide-area surface subsidence and the relationship between surface subsidence and influencing factors. In detecting land subsidence, SBAS-InSAR is widely used, based on the following equations (Berardino *et al.*, 2002):

$$\frac{N+1}{2} \leq M \leq N\left(\frac{N+1}{2}\right) \quad (1)$$

$$\Phi_j(x,r) = \Phi(t_B,x,r) - \Phi(t_A,x,r) \approx \Delta\Phi_{disp} + \Delta\Phi_{topo} + \Delta\Phi_{orb} + \Delta\Phi_{atm} + \Delta\Phi_{noise} \quad (2)$$

Equation (1) is a quantity range of M differential interferograms produced in the same area by N+1 SAR image at a specified time $(t_0, t_1, \ldots, t_n)$. Furthermore, Equation (2) represents the interferometric composition of the j (to be generated with two images in t_B and t_A) interferogram phase in pixels (x, r) where x and r are the respective azimuth and range co-ordinates. The change of distance from target to radar along the sight line (LOS) causes the phase $\Delta\Phi_{disp}$. Moreover the phases of $\Delta\Phi_{topo}$, $\Delta\Phi_{orb}$, $\Delta\Phi_{atm}$, and $\Delta\Phi_{noise}$ are created through the ground and satellite orbit, effect of the atmosphere and other noise, and in particular the effect of tropospheric delay. In order to achieve deformation process $\Delta\Phi_{disp}$ function, SBAS-InSAR remove the residual components from the interferometric phase.

3. RESEARCH METHODOLOGY

The study area of this research is Opak Fault, located in Yogyakarta Province, Indonesia. The data that was used here is Sentinel-1 InSAR data from 2016-2019, which was downloaded from COMET-LiCS web portal. The frame ID that was used is 076D_09725_121107. The study area can be seen in Figure 1. We used the following coordinates to be the boundary of the study area: 110.22° E, 110.55° E, -8.17° S, and -7,72° S. The total number of InSAR images in this study are 114.

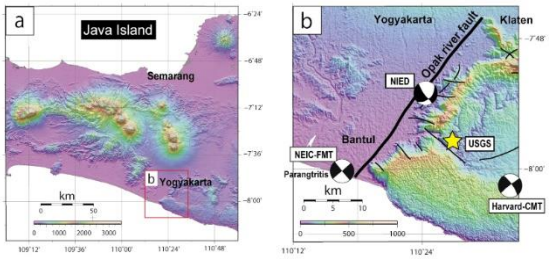

Figure 1. Study Area (modified from Tsuji *et al*., 2009)

We used the LiCSBAS software that was published by Morishita *et al.* (2020) to process the Sentinel-1 InSAR data. Our InSAR time series processor's LiCSBAS workflow is largely divided into two parts: preparing a stack of unwrapped data, and analyzing time series. LiCSBAS begins downloading the items from LiCSAR covering the region of interest and is accompanied by conversion of data format. Tropospheric noise correction using the InSAR (GACOS) data from the external Generic Atmospheric Correction Online Service (Yu *et al.*, 2018) and the masking / clipping of unwrapped data are optional measures that can be taken to improve accuracy and make processing more effective. To extract stratification and turbulent signals from tropospheric total delays, GACOS uses Iterative Tropospheric Decomposition (ITD) model (Yu *et al.* 2017), and create high resolution zenith total delays maps to be used for the correction of InSAR measurements and other applications. In the study of the time series, incorrectly unwrapped data is detected and discarded based on the accuracy and coverage of the unwrapped data and by checking the closure of the loop. In terms of SB interferograms, the STD of unwrapped phases for each entire interferogram is generally reduced (from 6.7 rad to 4.2 rad on average, from 6.0 rad to 3.9 rad on median), which indicates the GACOS correction significantly mitigated the tropospheric noise (Morishita *et al.*, 2020). The refined stack of unwrapped data is inverted to obtain the time series and velocity displacement, followed by the calculation of the standard velocity deviation (STD) and the masking of noisy pixels based on multiple noise indices. Finally, to minimize the residual noise and extract the filtered time series and velocity, a spatiotemporal filter is applied to the time series.

Interferograms are automatically generated in the LiCSAR processing chains on a predefined LiCSAR frame base (typically consisting of 13 explosions on each of the three IWS-mode subswaths corresponding to an area of 250 km x 250 km). Newly acquired data is co-recorded into a single primary image using a secondary auxiliary

image (closer to the latest image for the preservation of coherence) which has already been co-registered (if available) with an improved method for spectral diversity (Scheiber *et al.*, 2000). The interferograms will then be used, by default, for each acquisition with three preceding and three following acquisitions, although the number could be increased in the future. The interferograms are spatially filtered to minimize noise using a GAMMA adaptive spectrum filter with an alphha-value of 1.0 (Goldstein and Werner, 1998) and are multi-looked with a factor of 20 x 4 in range x azimuth (46 x 56 m spacing).

We perform an SB inversion on the interferogram network to estimate the velocity of a surface pixel over time based on a series of displacement results. Assume we have a stack of M-unwrapped interferograms $d = [d_1, \dots, d_M]^T$ rendered from N images acquired at $(t_0, \dots, t_{N-1})$, N-1 incremental displacement vector $m = [m_1, \dots, m_{N-1}]^T$ (i.e., m_i is the incremental displacement between time t_{i-1} and t_i) can be extracted by solving Equation (3):

$$d = Gm \tag{3}$$

Where G is a *M x (N-1)* zero architecture matrix representing the interferogram network relationship with incremental displacements, given that the unwrapped interferogram (i.e. displacement between two acquisitions) is the sum of the corresponding incremental displacements (Schmidt *et al*, 2003). For each acquisition, cumulative displacements (i.e., the displacement time series) are determined simply by summing the incremental displacement. The mean velocity of displacement is then calculated from the accumulated at least-square displacements.

We adopt the NSBAS approach (Agram *et al.*, 2019), which imposes a temporary limitation, to obtain the more practical time series of the displacement even with a disconnected network,

$$\begin{bmatrix} \mathbf{d} \\ \mathbf{0} \end{bmatrix} = \gamma \begin{bmatrix} \begin{bmatrix} & \mathbf{G} & & \mathbf{0} & \mathbf{0} \end{bmatrix} \\ \begin{bmatrix} 1 & 0 & \dots & \dots & 0 & -t_1 & -1 \\ \vdots & \ddots & \ddots & & \vdots & -t_2 & \vdots \\ 1 & \dots & 1 & \ddots & \vdots & \vdots & \vdots \\ \vdots & & \vdots & \ddots & 0 & \vdots & \vdots \\ 1 & \dots & 1 & \dots & 1 & -t_{N-1} & -1 \end{bmatrix} \end{bmatrix} \begin{bmatrix} \mathbf{m} \\ v \\ c \end{bmatrix} \tag{4}$$

where γ is a temporal constraint scaling (weighting) element and we assume that the displacement is linear ($d = vt+c$). Solutions within the network's linked parts are minimally influenced by the temporal restriction that provided that γ is low (e.g. 0.0001). Therefore, the temporal restriction component only affects the link through network gaps. For pixels with completely connected networks, as well as those with gaps, Equation (4) can thus be used.

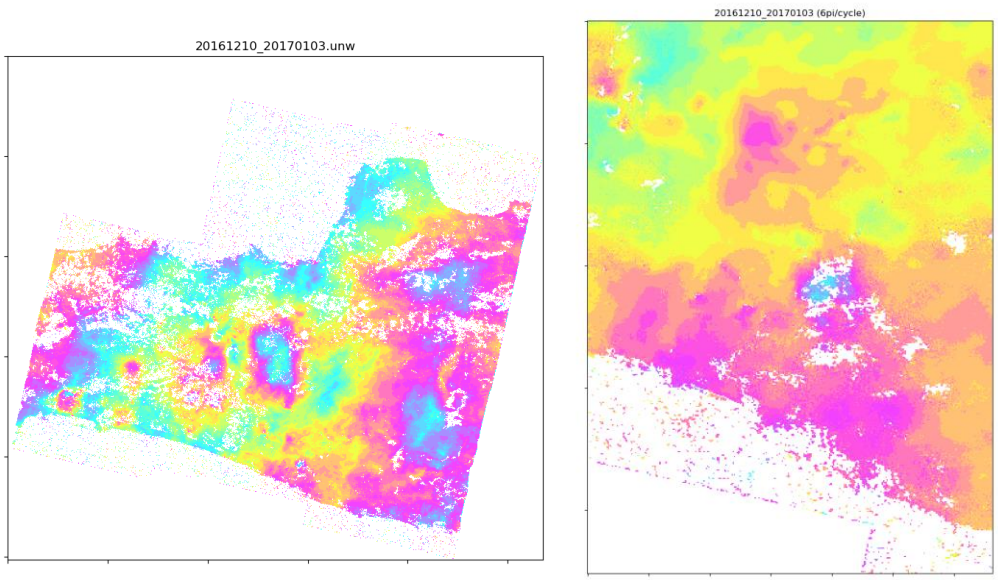

(a) (b)

Figure 2. Unwrapped Data

4. RESULTS AND DISCUSSIONS

4.1 Sentinel-1 InSAR Unwrapped Phase

The downsample is to convert GeoTIFF file process to single-precision floating-point format without header for further analysis of the time series, as well as downsamples (multilooks) data if defined by -n option. Examples of unwrapped phases are given in Figure 2. Figure 2a clarified the full unwrapped phase of Sentinel-1 InSAR, while Figure 2b shows the unwrapped phase of the clip using the particular region around the fault of Opak.

4.2 Loop Closure

Sets of three interferograms and defines bad data with major unwrapping errors that the loop phases are to be omitted from further processing performance. In the right bottom picture, non-zero (i.e., not light blue) areas mean that one (or more) of the three interferograms contain unwrapping errors there. Fortunately, no interferograms have major unwrapping errors in this case and will be removed at this stage.

4.3 Mask Time Series

This phase produces a mask for the displacement time series and velocity using multiple noise indices derived at previous steps. If any of the noise indices values for a pixel are greater / smaller than a specified threshold, the pixel will be masked. The mask time series can be seen in Figure 3. In that figure, coh avg is average of coherence, n unw is number of used unwrapped data, vstd is standard deviation of velocity (mm/yr), maxTlen is max time length of the connected network (year), n gap is number of gaps in the network, stc is spatio-temporal consistency (mm) (Hanssen *et al.*, 2008), n ifg noloop is a number of interferograms with no loops, n loop err is a number of unclosed loops, and resid is RMS of residuals in SB inversion (mm). The masked/unmasked velocity and mask are shown at the top raw, and the other images are indices of noise. The number indicated in the parentheses next to the titles of each noise index is the threshold used.

4.4 Time Series and Velocity Field Analysis

There are also some noise terms in the derived time series, including residual tropospheric noise, ionospheric noise, and orbital errors which are typically spatially associated and temporally uncorrelated. A spatiotemporal filter (i.e. high-pass in time and low-pass in space) can be used to attempt to isolate these noise components from the time series for displacement (Hooper *et al.*, 2012). To accomplish this filtering, we add, respectively, a one- and two-dimensional Gaussian kernel in time and space.

Interpretation of the derived time series is just as important as the exact time-series derivation. LiCSBAS is fitted with two windows (graphical user interfaces) consisting of an interactive time series display. The first picture window shows size, cumulative displacements and noise indices (Figure 4). In the second time series window (Figure 5) the corresponding time series with and without the spatiotemporal filter is plotted promptly when clicking on a pixel of interest.

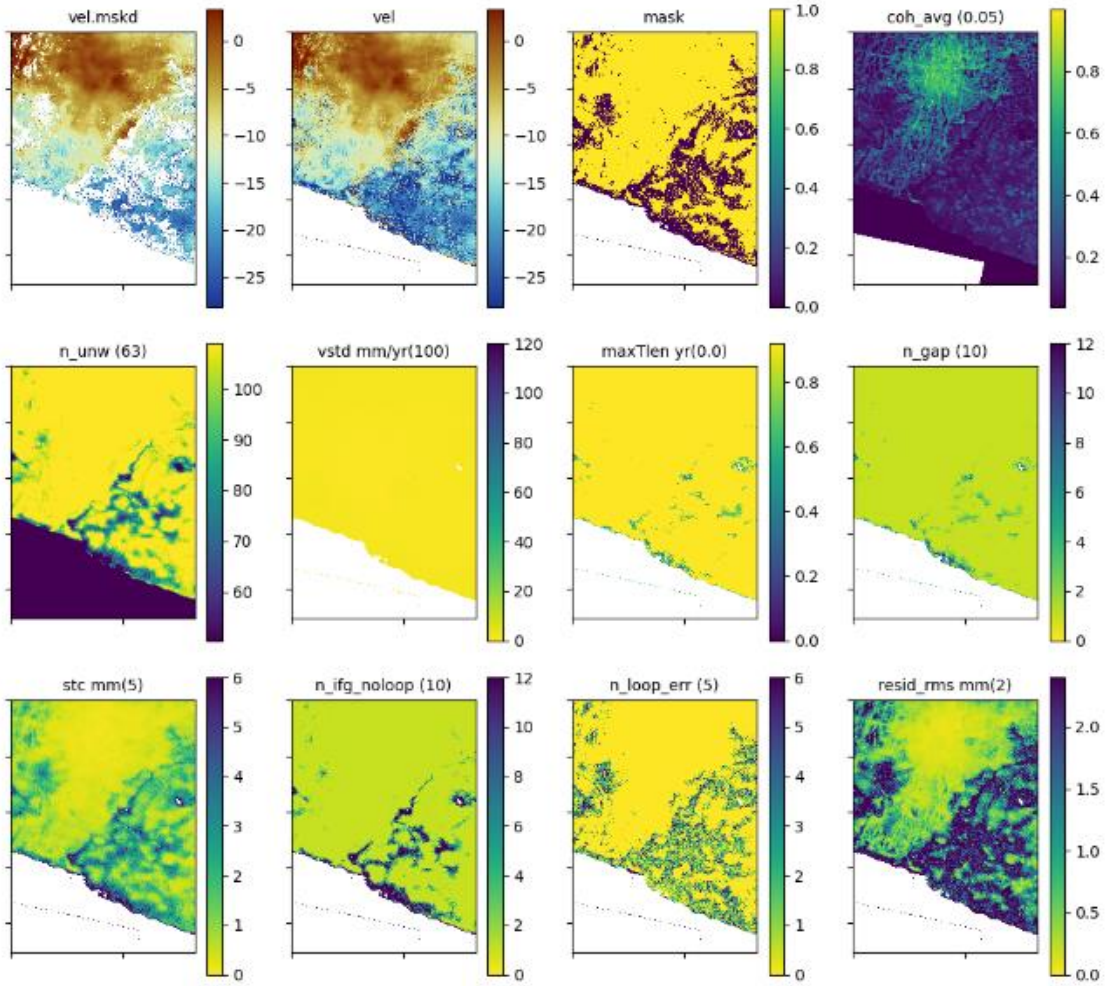

Figure 3. The Mask Time Series

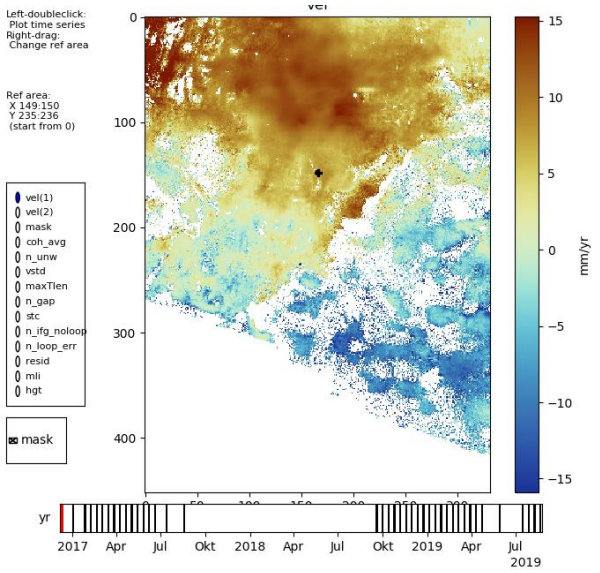

Figure 4. The deformation velocity maps around Opak Fault area

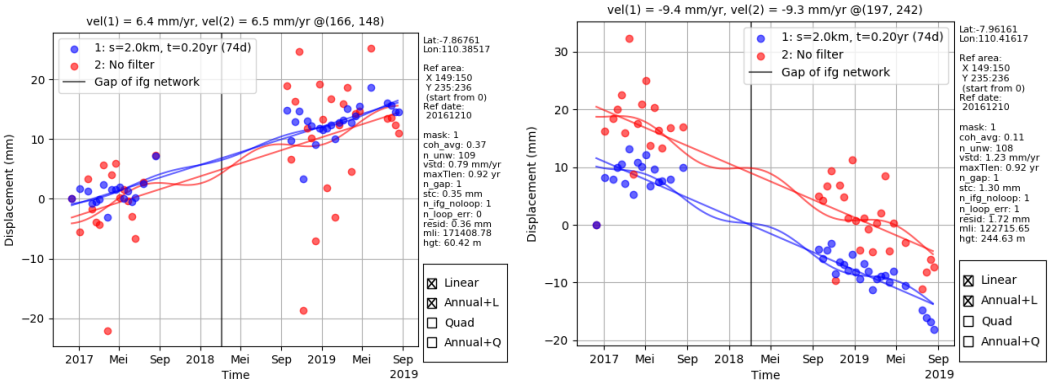

(a) (b)

Figure 5. The time series of deformation map. (a) Uplift movement in west area of Opak Fault and (b) Subsidence movement in east area of Opak Fault

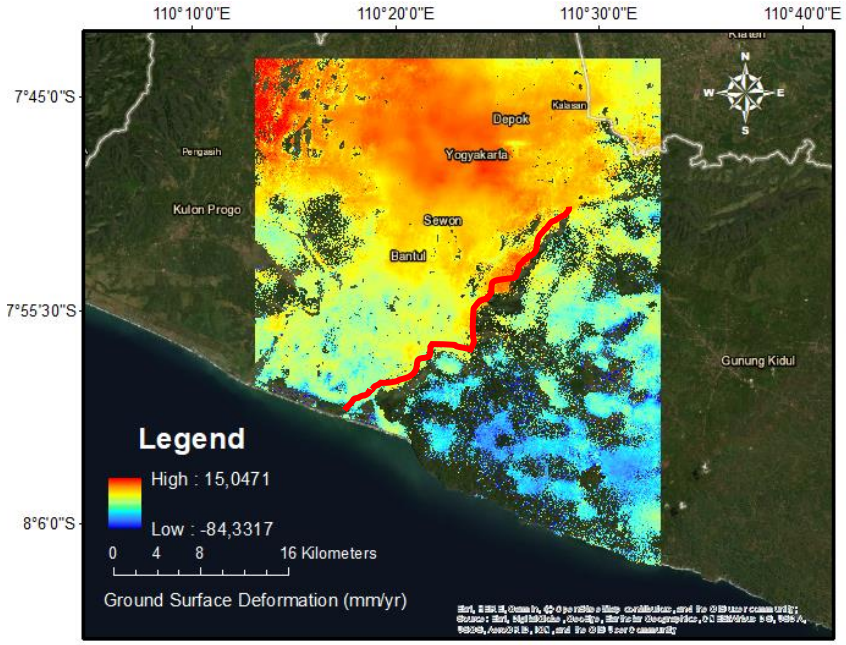

Figure 6. The deformation phenomenon with the base map. The red line shows the Opak Fault location.

The time-series showed by Figure 5a means uplift movement, while the subsidence was detected in Figure 5b with the number of ~15 mm/yr and ~30 mm/yr, respectively. If we see the Figure 6, it is clear to see that the deformation pattern occurred in around Opak Fault. Overall, the deformation ranges from -84 mm/yr to 15 mm/yr. The standard deviation of the deformation is 0.1 mm/yr. It can be checked in Figure 3 (vstd part image).

The west of Opak Fault shows the uplift movement. If we see more detail, the uplift movement in around beach area is smaller compared to the uplift movement in around Mount Merapi. This event can be caused by the subduction force in the south of Java Island and the magmatic process occurred in Mount Merapi. The subduction zone slowed the uplift movement, but the magmatic process in Mount Merapi add the uplift movement. However, in the east of Opak Fault, which is Gunungkidul Mountain, show the subsidence movement. Gunungkidul is an area which has a lot of caves which produce the sinkhole process. The subsidence phenomenon can be influenced by the cave and sinkhole process.

5. CONCLUSIONS

The objective of this study is to monitor the deformation in around Opak Fault. The location of the fault can be detected clearly and is visualized in Figure 6. The deformation that occurred in the west area of Opak Fault is uplift movement (~15 mm/yr), while in the east area is subsidence movement (~30 mm/yr). The uplift and subsidence movements are proved by the timeseries which is in Figures 5a and 5b. However, -84 mm/yr to 15 mm/yr are the deformation range detected around Opak Fault with the standard deviation of 0.1 mm/yr. It is important to understand the deformation that occurred in around Opak Fault because this fault is the source of Yogyakarta 2006 earthquake, which means that this fault is still very active.

ACKNOWLEDGEMENT

The authors would like to thank the LiCSBAS which give the permission to process the Sentinel-1 InSAR data in frame 076D_09725_121107. LiCSAR contains modified Copernicus Sentinel data [Year of data used] analysed by the Centre for the Observation and Modelling of Earthquakes, Volcanoes and Tectonics (COMET). LiCSAR uses JASMIN, the UK's collaborative data analysis environment (http://jasmin.ac.uk).

REFERENCES

Abercrombie, R.E., Antolik, M., Felzer, K., and Ekström, G., 2001. The 1994 Java tsunami earthquake: slip over a subducting seamount. *J. Geophys. Res., Solid Earth* 106, 6595–6607. https://doi.org/10.1029/2000JB900403.

Abidin, H.Z., Andreas, H., Meilano, I., Gamal, M., Gumilar, I., and Abdullah, C.I., 2009. Deformasi Koseismik dan Pascaseismik Gempa Yogyakarta 2006 dari Hasil Survei GPS. *Jurnal Geologi Indonesia*, 4(4):275-284. DOI: 10.17014/ijog.v4i4.87.

Agram, P., Jolivet, R., and Simons, M., 2019. Generic InSAR Analysis Toolbox (GIAnT)—User Guide. Available online: http://earthdef.caltech.edu(accessed on 27 November 2019).

Atzori, S., Hunstad, I., Chini, M., Salvi, S., Tolomei, C., Bignami, C., Stramondo, S., Trasatti, E., Antonioli, A., and Boschi, E., 2009. Finite fault inversion of DInSAR coseismic displacement of the 2009 L'Aquila earthquake (central Italy). *Geophys. Lett*., 36. https://doi.org/10.1029/2009GL039293.

Berardino, P., Fornaro, G., Lanari, R., and Sansosti, E., 2002. A new algorithm for surface deformation monitoring based on small baseline differential SAR interferograms. *IEEE Trans. Geosci. Remote Sens.*, 40, 2375–2383. DOI: 10.1109/TGRS.2002.803792.

Goldstein, R.M. and Werner, C.L., 1998. Radar interferogram filtering for geophysical applications. *Geophys. Res. Lett.*, 25, 4035–4038. DOI: 10.1029/1998GL900033.

Hamilton, W., 1979. Tectonics of the Indonesian Region. *United States Geological Survey*, 1078, 345 p. https://doi.org/10.3133/pp1078.

Hanssen, R.F., van Leijen, F.J., van Zwieten, G.J., Bremmer, C., Dortland, S., and Kleuskens, M., 2020. Validation of existing processing chains in TerraFirma stage 2. Product validation: Validation in the Amsterdam and Alkmaar area Draft version 3. 2008. Available online:https://raw.githubusercontent.com/wiki/yumorishita/LiCSBAS/documents/Hanssen_2008.pdf(accessed on 27 January 2020).

Hooper, A.J., Bekaert, D., Spaans, K., and Arikan, M., 2012. Recent advances in SAR interferometry time series analysis for measuring crustal deformation. *Tectonophysics*, 514–517, 1–13. https://doi.org/10.1016/j.tecto.2011.10.013.

Lanari, R., Casu, F., Manzo, M., and Lundgren, P., 2007. Application of the SBAS-DInSAR technique to fault creep: A case study of the Hayward fault, California. *Remote Sens. Environ*., 109, 20–28. DOI: 10.1016/j.rse.2006.12.003.

Lay, T., 2015. The surge of great earthquakes from 2004 to 2014. *Earth Planet. Sci. Lett.* 409, 133–146. https://doi.org/10.1016/j.epsl.2014.10.047.

Loveless, J.P. and Meade, B.J., 2010. Geodetic imaging of plate motions, slip rates, and partitioning of deformation in Japan. *J. Geophys. Res., Solid Earth* 115, B02410. https://doi.org/10.1029/2008JB006248.

Manunta, M., Marsella, M., Zeni, G., Sciotti, M., Atzori, S., and Lanari, R., 2008. Two-scale surface deformation analysis using the SBAS-DInSAR technique: A case study of the city of Rome, Italy. *Int. J. Sens.* 2008, 29, 1665–1684. https://doi.org/10.1080/01431160701395278.

Massonnet, D. and Feigl, K.L., 1998. Radar interferometry and its application to changes in the Earth's surface. *Rev. Geophys*., 36, 441–500. https://doi.org/10.1029/97RG03139.

Morishita, Y., Lazecky, M., Wright, T.J., Weiss, J.R., and Elliott, J.R., 2020. LiCSBAS: An Open-Source InSAR Time Series Analysis Package Integrated with the LiCSAR Automated Sentinel-1 InSAR Processor.

Remote Sens., 12, 424. DOI: 10.3390/rs12030424.

Newcomb, K.R. and McCann, W.R., 1987. Seismic history and seismotectonics of the Sunda arc. *J. Geophys. Res., Solid Earth*, 92, 421–439. https://doi.org/10.1029/JB092iB01p00421.

Poland, M., 2010. Localized Surface Disruptions Observed by InSAR during Strong Earthquakes in Java and Hawai'i. *Bulletin of the Seismological Society of America*, 100 (2), pp. 532–540. DOI: 10.1785/0120090175.

Scheiber, R. and Moreira, A., 2000. Coregistration of interferometric SAR images using spectral diversity. *IEEE Trans. Geosci. Remote Sens.*, 38, 2179–2191. DOI: 10.1109/36.868876.

Schmidt, D.A. and Bürgmann, R., 2003. Time-dependent land uplift and subsidence in the Santa Clara valley, California, from a large interferometric synthetic aperture radar data set. *J. Geophys. Res. Solid Earth*, 108, 1–13. https://doi.org/10.1029/2002JB002267.

Trasatti, E., Casu, F., Giunchi, C., Pepe, S., Solaro, G., Tagliaventi, S., Berardino, P., Manzo, M., Pepe, A., and Ricciardi, G.P., 2008. The 2004-2006 uplift episode at Campi Flegrei caldera (Italy): Constraints from SBAS-DInSAR ENVISAT data and Bayesian source inference. *Geophys. Lett.*, 35. DOI: 10.1029/2007GL033091.

Tsuji, T., Yamamoto, K., Matsuoka, T., Yamada, Y., Onishi, K., Bahar, A., Meilano, I., and Abidin, H.Z., 2009. Earthquake fault of the 26 May 2006 Yogyakarta earthquake observed by SAR interferometry. *Earth Planets Space*, 61, e29–e32. DOI: 10.1186/BF03353189.

Wallace, L.M. and Beavan, J., 2010. Diverse slow slip behavior at the Hikurangi subduction margin, New Zealand. *J. Geophys. Res., Solid Earth* 115, B12402. https://doi.org/10.1029/2010JB007717.

Yu, C., Penna, N. T., and Li, Z., 2017. Generation of real-time mode high-resolution water vapor fields from GPS observations. *J. Geophys. Res. Atmos.*, 122, 2008–2025, DOI: 10.1002/2016JD025753.

Yu, C., Li, Z., Penna, N.T., and Crippa, P., 2018. Generic Atmospheric Correction Model for Interferometric Synthetic Aperture Radar Observations. *J. Geophys. Res. Solid Earth*, 123, 9202–9222. https://doi.org/10.1029/2017JB015305.

Xu, B., Feng, G., Li, Z.-W., Wang, Q., Wang, C., and Xie, R., 2016. Coastal Subsidence Monitoring Associated with Land Reclamation Using the Point Target Based SBAS-InSAR Method: A Case Study of Shenzhen, China. *Remote Sens.*, 8, 652. DOI: 10.3390/rs8080652.

Zeni, G., Bonano, M., Casu, F., Manunta, M., Manzo, M., Marsella, M., Pepe, A., and Lanari, R., 2011. Long-term deformation analysis of historical buildings through the advanced SBAS-DInSAR technique: The case study of the city of Rome, Italy. *J. Geophys. Eng.*, 8, S1–S12. DOI: 10.1088/1742-2132/8/3/S01.

Zhou, L., Guo, J., Hu, J., Li, J., Xu, Y., Pan, Y., and Shi, M., 2017. Wuhan Surface Subsidence Analysis in 2015–2016 Based on Sentinel-1A Data by SBAS-InSAR. *Remote Sens.*, 9, 982. DOI: 10.3390/rs9100982